Journal of Current Science and Technology, April-June 2026 Vol. 16 No. 2, Article 177

ISSN 2630-0656 (Online)

Cite this article: Hapsari, R. I., Putri, F. S., Harsanti, W., Nugroho, G. A., Nurlatifah, A., Awaludin, A., & Halim, H. B. A. (2026). Effects of land use change and climate projections on erosion and sediment transport in the Kricik River Basin, Indonesia: A modeling study. *Journal of Current Science and Technology*, *16*(2), Article 177. https://doi.org/10.59796/jcst.V16N2.2026.177

Journal of Current Science and Technology

Journal homepage: https://jcst.rsu.ac.th

Effects of Land Use Change and Climate Projections on Erosion and Sediment Transport in the Kricik River Basin, Indonesia: A Modeling Study

Ratih Indri Hapsari[1], Fidia Sabilla Putri[2,*], Winda Harsanti[1], Ginaldi Ari Nugroho[3], Amalia Nurlatifah[3], Asif Awaludin[3], and Hazruwani Binti A Halim[4]

[1]Department of Civil Engineering, Politeknik Negeri Malang, Malang, Indonesia
[2]Department of Water Resources Engineering, Faculty of Engineering, Universitas Brawijaya, Indonesia
[3]National Research and Innovation Agency, Indonesia
[4]Politeknik Sultan Salahuddin Abdul Aziz Shah, Malaysia

*Corresponding author; E-mail: fidiasabillaptr@student.ub.ac.id

Received 2 July 2025; Revised 11 October 2025; Accepted 27 November 2025; Published 7 April 2026

Abstract

This research assessed the effects of land use change and climate change on the rates of erosion and sediment transport volumes. To quantify erosion and sediment mobilization, the Modified Universal Soil Loss Equation was applied in conjunction with sediment transport analysis. Precipitation projections from the Community Earth System Model Version 2 under the Shared Socioeconomic Pathway SSP2-4.5 scenario were employed to evaluate future climate impacts. Model validation was improved using high-resolution Unmanned Aerial Vehicle (UAV) footage. The study area was the Kricik River watershed, located in East Java, Indonesia. This watershed strongly affects the hydrological and sedimentary processes of the broader Brantas River basin. A comparative analysis of land use across 2010, 2021, and 2025 revealed a decline in forest and plantation cover, accompanied by an increase in dryland and urban development. Under the 2021 condition, the design peak discharge increased from 22.82 m^3/s to 24.97 m^3/s, while sediment yield rose to 101.94 tons, up from 75.21 tons in 2010. Climate change forecasts for 2026–2060 under SSP2-4.5 showed a substantial increase in hydrological and geomorphological hazards, with the expected peak discharge estimated at 30.83 m^3/s. The sediment yield in this scenario escalated to 129.05 tons, whereas the capacity of debris flow transport increased from 80,596.71 m^3 to 99,484.95 m^3. The study provides actionable insights for watershed managers and policymakers, highlighting the importance of climate adaptation and sustainable land use planning to alleviate future hazards of erosion, sedimentation, and flooding. The findings emphasize that policymakers should prioritize the development and enforcement of land use zoning regulations and watershed conservation policies that limit impervious surface expansion, encourage reforestation or agroforestry, and protect upstream buffer zones to control runoff coefficients.

Keywords: *erosion; sedimentation; Kricik River; land use; MUSLE; climate change*

1. Introduction

Erosion and sedimentation are dynamic processes that shape landscapes and affect water resources, agricultural productivity, and infrastructure integrity (Pumpuang & Aobpaet, 2024). These processes are influenced by land use change and climate change (Yang et al., 2003). Deforestation, urbanization, and agricultural expansion alter vegetation cover, soil characteristics, and runoff dynamics, resulting in increased soil erosion and sediment transport. Extreme rainfall events, which exacerbate runoff phenomena, and temperature variations influence the hydrological processes affecting the erosion and sedimentation dynamics (Dash & Maity, 2023; Kulkarni, 2021).

The Brantas River is a crucial river system in East Java, Indonesia, providing essential water for farming, hydropower, and domestic consumption (Wiwoho et al., 2024). In this watershed, these dual pressures are evident, largely driven by tourism growth. In 2021, the Kricik River experienced a catastrophic sediment-laden flash flood, resulting in fatalities and considerable property destruction (Putri et al., 2022). However, many tributaries in the Upper Brantas River remain ungauged, making hydrological data limited and difficult to predict.

It is important to integrate modeling tools, such as remote sensing, Geographic Information System (GIS)-based analysis, and process-based erosion models, to understand and mitigate the long-term consequences of environmental changes (Leh et al., 2013; Mohammadi et al., 2021). To understand and anticipate the environmental consequences of human actions, some researchers have simulated the effects of land use change on erosion and sedimentation (Li et al., 2022; Xiao et al., 2023). However, understanding of the non-linear responses of soil erosion and sediment transport under extreme conditions remains insufficient (Borrelli et al., 2021; Faksomboon, 2023).

Comprehensive studies that directly quantify the impact of land use changes on erosion and sedimentation processes remain scarce (Hernina et al., 2024). Additional research is required to enhance the adaptability of hydrological and erosion models to evolving climate conditions. Lack of direct observational data remains a significant challenge in hydrological modeling (Lagogiannis & Dimitriou, 2021). Therefore, direct observations and unmanned aerial vehicles can play a crucial role in filling data gaps and enhancing accuracy (Acharya et al., 2021).

2. Objectives

This study aimed to examine the impact of land use change and climate change on erosion and sedimentation in the Kricik River Basin, a sub-watershed of the Brantas River in East Java, Indonesia. Specifically, the study sought to: (1) quantify erosion rates and sediment yield across historical land use conditions (2010, 2021, and 2025) using the Modified Universal Soil Loss Equation (MUSLE) and GIS-based analysis; (2) project future hydrological and sediment transport responses through 2060 using CESM2 climate projections under the SSP2-4.5 scenario and the Takahashi sediment transport model; (3) validate model outputs against high-resolution UAV imagery; and (4) contribute to the development of resilience strategies for sustainable land use planning, flood risk mitigation, and watershed management in the region.

3. Materials and Methods

3.1 Study Area

The study was conducted in the Kricik River Basin, a sub-watershed within the Upper Brantas River Basin in East Java Province, Indonesia. The study area was located within the administrative boundaries of Batu City, which is renowned for its diverse agricultural activities, particularly horticulture and fruit cultivation. The Kricik River Basin spans a total area of 13.82 km², with the main river extending for 7.88 km. Water flow from tributaries to the main river in the basin is characterized by an elongated watershed and a dendritic drainage pattern. The river does not have a constant daily flow and is classified as an intermittent river.

The sediment transport and flood dynamics of the basin are influenced by human activities and the high variability of rainfall, which is mainly controlled by seasonal monsoons. The region is particularly susceptible to erosion due to the presence of loose volcanic soil and steep slopes (Ray et al., 2023; Nassor et al., 2025). The study area is illustrated in Figure 1. In 2021, the river was struck by a flash flood. The flood event, induced by intense rainfall that reached as much as 80.2 mm within two hours, led to the significant transport of substantial quantities of mud, debris, and sediment downstream. The flood caused the loss of several lives and the displacement or injury of numerous people. Figure 2 captures the aftermath of the catastrophic sediment-laden flood along the Kricik River.

3.2 Spatial Data

The spatial data used in this study included land use, a topographic map, a soil type map, and climate change data. Topographic data were obtained from Ina-Geoportal and combined with UAV survey results to generate detailed contours. Soil data were sourced from the Food and Agriculture Organization (FAO) Soils Portal. The historical land use information for 2010 was obtained from Ina-Geoportal and verified through interviews with the Public Works Office, while the 2021 and 2025 land use data were obtained from Google Earth satellite imagery processed using SASPlanet. Figure 3 shows the topographic map, land use map, and soil map delineated for the Kricik River Basin.

3.3 Hydrological and Climate Data

The hydrological data used for flood event simulations were annual maximum daily rainfall data from the nearest rainfall stations: Ngujung Station, Tinjomoyo Station, and Junggo Station (black dots in Figure 1). Ground-based stations offer more precise data than satellite estimates in complex terrains such as the Kricik River Basin, where orographic effects substantially influence rainfall distribution.

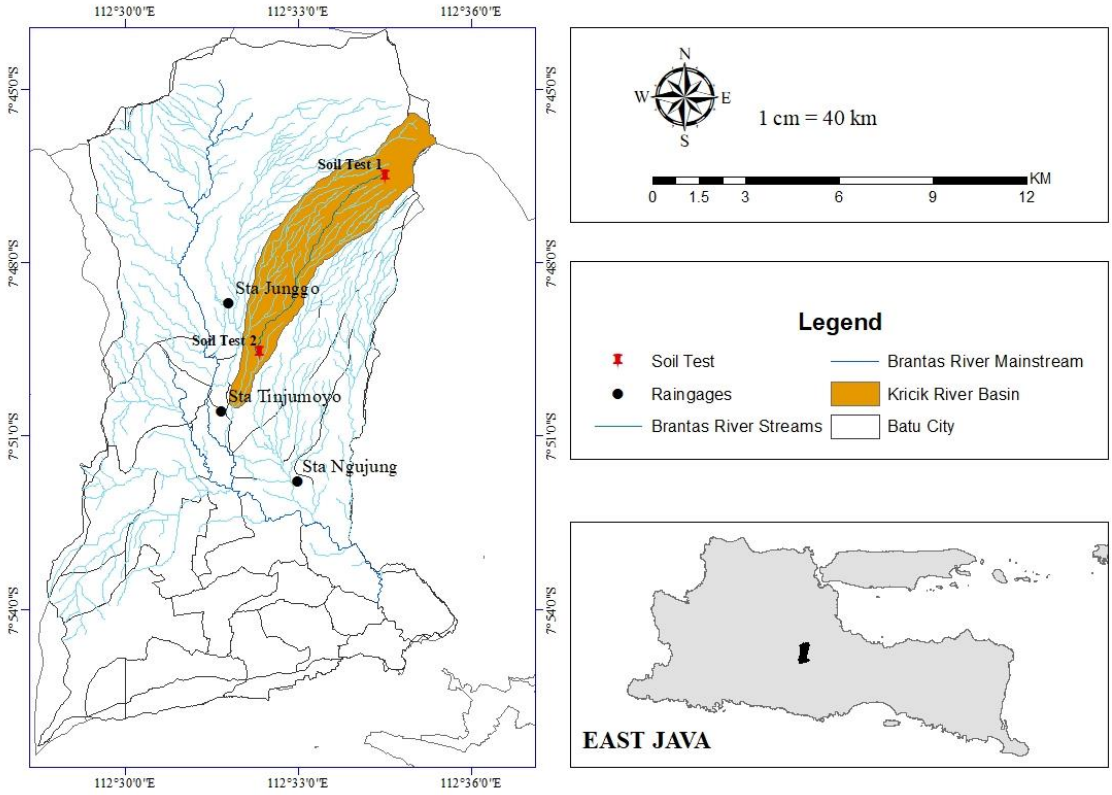

Figure 1 Map of the study area (Batu City), locations of rain gauges, soil sampling sites, and the catchment area

Figure 2 Photograph of flooding in the Kricik River
Adapted from https://www.antaranews.com/berita/2506385/seluruh-korban-banjir-bandang-kota-batu

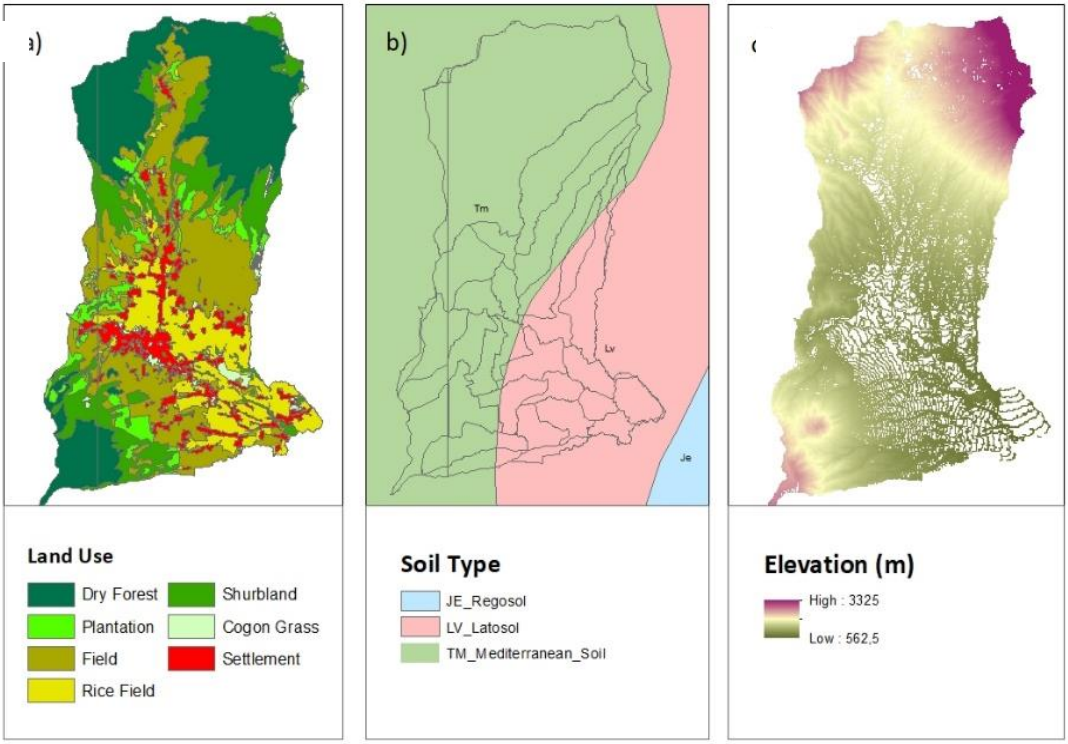

Figure 3 Spatial data layers delineated for the Kricik River Basin: land use map for 2021 (a), soil type map (b), and topographic elevation map (c).

Climate change projections were obtained from CESM2 through the University Corporation for Atmospheric Research. CESM2 is a fully coupled community global climate model that provides state-of-the-art computer simulations of the Earth's past, present, and future climate states (Danabasoglu et al., 2020). The variable used in this study was precipitation (Pr), defined as the precipitation amount over 24 hours. The selected parameter for climate change analysis was the projected design rainfall up to the year 2060.

Due to the systematic inaccuracies inherent in climate change models, data from various global sources must be adjusted for bias. The delta change anomaly was computed for each projected year by comparing the CESM2-simulated precipitation against the model's own historical baseline, and the resulting relative deviation was applied annually as a multiplicative adjustment factor to the observed rainfall record. The adjustment factor consisted of the relative deviations in rainfall applied throughout all months, following the Copernicus Climate Change Service's Info Sheets. The rainfall raster data had to be spatially downscaled to represent regional rainfall variability over the Kricik River Basin. A linear regression approach was applied for spatial downscaling (Shu & Lam, 2011).

3.4 Soil Data

The soil information utilized in this study was obtained through direct field investigation and laboratory analysis of two soil samples taken from the upstream (7°46′33.53″S, 112°34′30.17″E) and downstream (7°49′35.13″S, 112°32′19.28″E) of catchment area (see Figure 3a). The soil investigation revealed that the samples were composed of varying proportions of sand, silt, and clay, with an average plasticity index of 18.03%, classifying them as highly plastic clay. The average proportions of silt and clay were 31.38% and 40.43%, respectively. According to the FAO Digital Soil Map of the World, the soil categories in the study area are Latosols, Mediterranean soils, and Regosols. The soil was somewhat poorly aggregated, with low resistance to erosion. Some organic material was found in the sediment averaging 4.00% indicating higher sediment cohesion. The average soil permeability was assessed as 1.26×10^{-9} m/s.

Laboratory tests were also conducted to characterize the debris material and to determine its

physical and mechanical properties. The average mass density was found to be 1.65 g/cm³, which corresponds to loose, fine-grained soil. Shear strength parameters were also evaluated, revealing an average static internal shear angle of 21.47°. The void ratio of the debris material was measured at an average of 0.40.

3.5 River Morphology Data

Kricik River morphology data were obtained from topographic maps and surveys. These data provide information about the river shape and dimensions, sedimentation conditions, structure, and physical characteristics of the river channel, which are essential for sediment transport analysis. Figure 4, left, shows photographs of the river in the upstream and disaster-affected areas. From the UAV photogrammetry, river width, depth, and cross-sectional profiles can be extracted (Figure 4, right).

3.6 Hydrological Analysis

This investigation employed the Nakayasu method to generate synthetic flood hydrographs. In regions where streamflow data are scarce, this method is frequently applied because it is based on readily available rainfall data and watershed characteristics (Kang et al., 2013). The method estimates the flood response of a catchment area using parameters that include catchment area, stream length, and runoff coefficient (*C*r) (Hidayat et al., 2022). This method was originally introduced by Nakayasu (1956) to estimate the peak discharge, q_p (m³/s), using the formula:

$$q_p = \frac{1}{3.6}\left(\frac{D.R_0}{0.3T_1 + T_{0.3}}\right) \quad (1)$$

where q_p is the flood peak (m³/s), D is the catchment area (km²), R_0 is the effective rainfall (mm), T_1 is the time to peak (h), and $T_{0.3}$ is the time to reach $0.3q_p$. Effective rainfall, which represents the portion of total rainfall that contributes to runoff and potential flooding, can be calculated from the daily distributed design rainfall following the Gumbel distribution with a 50-year return period.

Time lag, t_g (h) is

If L > 15 km, $t_g = 0.21\ L^{0.7}$ (2)

If L < 15 km, $t_g = 0.4 + 0.058\ L$ (3)

where L is the river length (km).

Time to peak, T_1 (h) is

$T_1 = t_g + 0.8\ t_r$ (4)

$t_r = (0.5 \sim 1.0)\ t_g$ (5)

where tr is the rainfall duration (h)

Time to reach $0.3q_p$ is

$T_{0.3} = a \times tg$ (6)

where a is the catchment parameter which is 1.5 for rivers that respond slowly to rainfall but recede quickly, 3 for rivers where the rise of discharge is fast, but the recession is slow, and 2 for the rivers with intermediate characteristics between the two.

The ordinate of the upward hydrograph, Q_a (m³/s) is:

$$\frac{Q_a}{q_p} = \left(\frac{t}{T_1}\right)^{2.4} \quad (7)$$

where t is the time step (h) which is the abscissa of hydrograph.

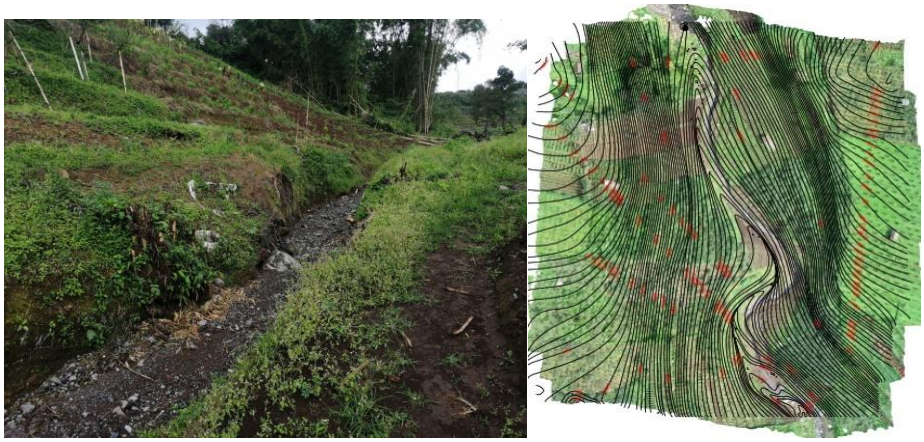

Figure 4 Kricik River photographs from the direct survey and topography from UAV

The ordinate of downward hydrograph is:

$$\text{For } \frac{q_d}{q_p} \geq 0.3,\ \frac{q_d}{q_p} = 0.3^{(t-T_1)/T_{0.3}} \quad (8)$$

$$\text{For } 0.3 > \frac{q_d}{q_p} \geq 0.3^{0.2},\ \frac{q_d}{q_p} = 0.3^{(t-T_1+0.5T_{0.3})/1.5T_{0.3}} \quad (9)$$

$$\text{For } 0.3^{0.2} > \frac{q_d}{q_p},\ \frac{q_d}{q_p} = 0.3^{(t-T_1+1.5T_{0.3})/2T_{0.3}} \quad (10)$$

where q_d is the discharge in downward unit hydrograph (m^3/s).

3.7 Erosion Rate

The MUSLE (Modified Universal Soil Loss Equation) method was employed in this study to analyze soil erosion, taking into account factors such as discharge, land use, land cover, and soil characteristics. The MUSLE equation (Williams, 1975) is as follows:

$$SY = 11.8(Q \times q_p)^{0.56} \times K \times LS \times Cm \times P \quad (11)$$

where SY is sediment yield (ton), Q is runoff volume (m^3), q_p is the peak runoff rate (m^3/s), K is the soil erodibility factor ([ton·km^2·s]/[km^2·ton·mm]), LS is the slope length and gradient factor, *C*m is the cropping management factor, and P is the erosion control practice factor.

Runoff volume and peak runoff rate, which play a key role in triggering soil erosion, were obtained from the synthetic flood hydrograph. The soil erodibility factor was included to ascertain the degree to which a soil type is susceptible to erosion because of human activity and rainfall. The K-factor was estimated to use a soil erodibility nomograph (Wischmeier & Smith, 1978) because of a series of laboratory tests on soil samples. The samples were tested for particle size distribution (sand, silt, clay concentration), organic matter, permeability, and onsite assessments of soil structure.

The LS factor represents the effect of slope length (L) and slope steepness (S) on soil erosion. It is calculated using the following formula (Wischmeier & Smith, 1978):

$$LS = \left(\frac{\lambda}{22.13}\right)^m \times (65.41 \sin 2\theta + 3.56 \sin\theta + 0.065) \quad (12)$$

where λ is slope length (m), θ is angle of slope, m is the slope factor (0.5 if the percent slope is 5% or more, 0.4 if the percent slope is 3.5% to 4.5%, and 0.2 for a uniform slope, or a slope of less than 1%).

Cropping management factor (C) shows the combined effect of various cover and management factors. It is defined as the ratio of soil loss from cultivated land under specific conditions compared to soil loss from bare land with no vegetation cover. The cropping management factor is determined from categorization for cropland, construction areas, pasture, range, idle land, undisturbed forest land, and woodland. The erosion control practice factor (P) varies as follows: contouring, strip cropping, and terracing with some specifications according to the guidelines suggested in Wischmeier and Smith (1978).

3.8 Sediment Transport

Since the river is an intermittent stream, the majority of sediment transport typically occurs during high-intensity events such as floods. The Takahashi method (Takahashi, 1977) was applied to analyze the formation of debris flow due to the effects of surface water runoff. The gradient of the riverbed and the type of sediment flow are contributing factors to the sediment volume. The critical slope $\tan\theta_d$ for stony debris flow initiation is formulated as follows (Takahashi, 2001):

$$\tan\theta_d = \frac{C^*(\rho_s - \rho_w)}{C^*(\rho_s - \rho_w) + \rho_w\left(1 + \frac{h_0}{ac}\right)} \tan\varphi \quad (13)$$

where C^* is maximum sediment concentration on the riverbed (about 0.65 for uniform natural grains), ρ_s is debris particle mass density (ton/m^3), ρ_w is water density (ton/m^3), ac is depth in the sediment layer (m), h_0 is water flow depth on the stream (m), and φ is internal friction angle (°). The critical slope gives a threshold condition: if the actual slope is greater than the critical slope, debris flow can occur.

In debris flows, the collective movement of particles is assumed to fill the entire depth, because all the material flows simultaneously, driven by gravitational and inertial forces. Therefore, the sediment concentration C_d (dimensionless) is considered the same for all depths and can be calculated using the Takahashi formula (Takahashi, 1978). When the riverbed gradient is greater than 20°, the concentration of debris flow is simply $0.9C^*$. The C^* is volumetric sediment concentration of the deposited sediment, which is about 0.6. When the riverbed gradient is below 20°, the concentration of debris flow can be estimated by the following equation:

$$C_d = \frac{\rho_w \cdot \tan\theta}{(\rho_s - \rho_w).(\tan\varphi - \tan\theta)} \quad (14)$$

where tanθ is the riverbed gradient. If Cd exceeds 0.9 C^*, the assigned value of C_s is $0.9C^*$ with minimum allowable value for C_d is 0.3.

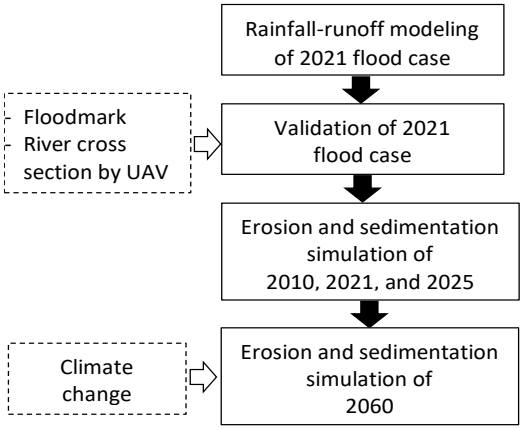

Figure 5 Research flow diagram

The volume of sediment carried in one flow, Vec (m^3) can be calculated using the empirical formula from (Mizuyama, 2008) as follows:

$$V_{ec} = \frac{R_{24} \times A \times 10^3}{1-\lambda}\left(\frac{C_d}{1-C_d}\right) \cdot f_r \quad (15)$$

where R24 is the maximum daily rainfall (mm/day), A is catchment area (km^2), λ is void ratio, fr is flow correction factor that depends on the catchment area (0 to 0.5).

3.9 Research Design

Figure 5 summarizes the methodological steps applied in the study. The process begins with rainfall-runoff modeling of the 2021 flood case, followed by validation using UAV-based floodmark and river cross-section data. Once validated, the model simulates erosion and sedimentation for the years 2010, 2021, and 2025 representing historical land use changes. A separate branch incorporates climate change scenarios, enabling the projection of erosion and sedimentation patterns for 2060. These two approaches integrate both empirical and future-oriented analyses to assess the combined impacts of land use and climate change.

Both MUSLE and Takahashi's sediment transport model are non-spatial models. In this study, both models were applied in a lumped manner, meaning that spatial variability within the watershed—such as slope gradient, land cover heterogeneity, and channel geometry is not explicitly represented in the simulations.

4. Results

4.1 Land Use Change

Figure 6 and Table 1 show the land use area for each category, comparing 2010, 2021, and 2025 conditions. Notably, there was no change in land use between 2021 and the projected conditions in 2025. Comparison with 2010 revealed substantial changes that were likely to affect the dynamics of erosion and sedimentation in the region. The decrease in forest cover from 719.14 ha to 569.05 ha was the most significant change. The decrease in forest area indicates that the landscape was more susceptible to erosion as a result of the absence of vegetative protection. Simultaneously, plantation area declined significantly from 81.04 ha to 20.69 ha, as former plantations were converted to grassland and shrubland, resulting in more exposed soil and reduced vegetative cover, which contributed to higher surface runoff and sediment transport. Additionally, the settlement area increased from 42.75 ha to 45.60 ha. Urbanization typically results in an increase in impervious surfaces, which in turn reduces infiltration and accelerates surface runoff. However, localized erosion rates may still be considerably influenced by specific management practices in former plantation areas, such as terracing or contouring.

Table 1 Land use area (ha) in 2010, 2021, and 2025

	2010	**2021**	**2025**
House	42.75	45.60	45.60
Plantation	81.04	20.69	20.69
Field	246.57	315.27	315.27
Grass	12.62	89.58	89.58
Shrubland	280.32	344.39	344.39
Dry Forest	719.14	569.05	569.05
Total		**1382.44**	

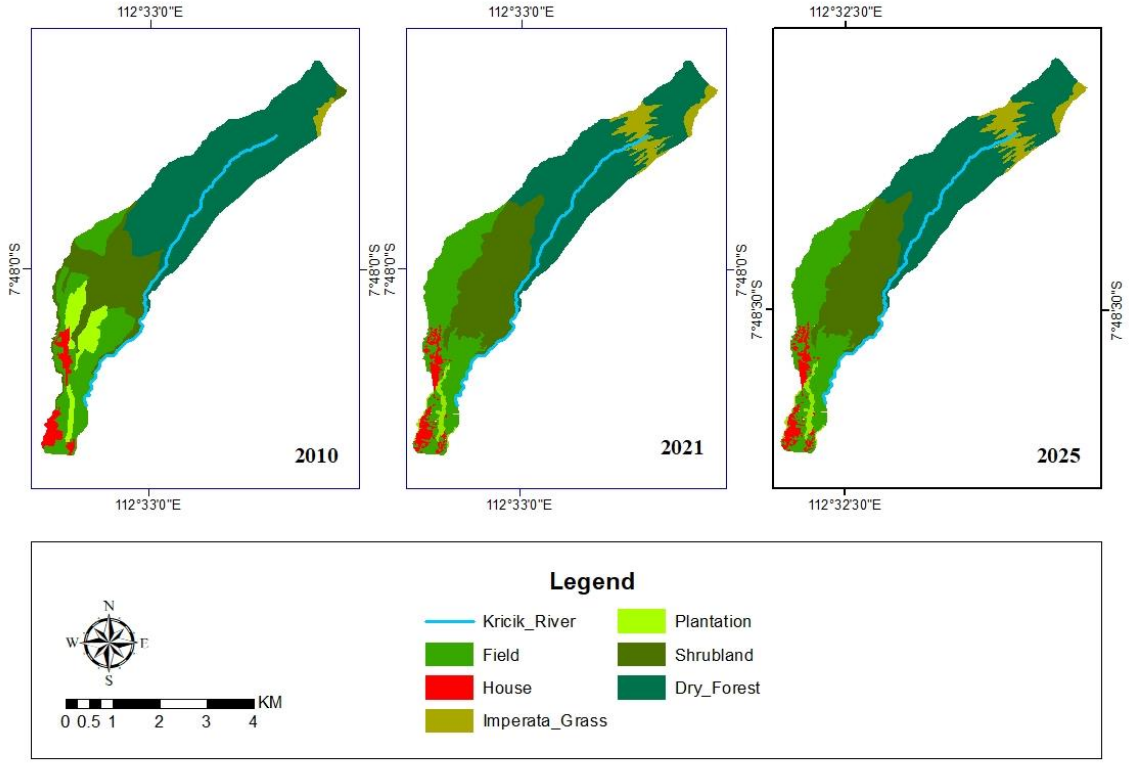

Figure 6 Land use map in 2010 (left), 2021 (middle), and 2025 (right)

4.2 Hydrological Analysis and Verification

The hydrological analysis provided the primary parameters used to estimate surface discharge in the study area. The design rainfall with a 50-year return period was determined to be 124.67 mm/day by intensity-duration-frequency (IDF) analysis using the Gumbel distribution of historical rainfall data from 2011 to 2024. The runoff coefficient (φ), calculated as a weighted average across each land use type in 2021, was 0.27. The effective rainfall, which represents the proportion of total rainfall that contributes to surface runoff, was estimated to be 33.27 mm/day. Based on flood analysis using the Nakayasu method, the time lag was 0.89 hours and the time to peak was 1.43 hours, resulting in a peak runoff discharge of 24.97 m^3/s.

In comparison to the 2021 and 2025 conditions, land use in 2010 resulted in lower flood potential due to less urban development, assuming constant rainfall. The runoff coefficient in 2010 was 0.24, indicating a smaller contribution to direct runoff. The estimated effective rainfall was 21.42 mm/day (64.4% of the 2021 value of 33.27 mm/day), and the peak runoff discharge was 22.82 m^3/s, lower than the 24.97 m^3/s simulated under 2021 land use conditions.

The severe storm event of 4 November 2021 was selected to verify the hydrograph analysis. Direct flow measurements were unavailable due to the absence of a discharge monitoring station along the river. Therefore, the runoff volume and peak discharge from the 2021 event were used to estimate river water depth by applying the Manning equation, with a roughness coefficient of 0.06 at the outlet point. The hydraulic calculation was based on flood marks recorded across five spatial locations (0+000 to 0+200), as presented in Table 2. The scatter plot in Figure 7 (right) presents a comparison between simulated and observed hydraulic discharge. The observed values ranged from 20.82 to 28.69 m^3/s, while the simulated values were consistently clustered around 24.97 m^3/s.

Table 2 Calculation of observed discharge based on flood marks

Point	Shape	Flood Mark	Cross Section Area (m^2)	Wet Perimeter (m)	Slope	Q Manning (m^3/s)	Q simulated (m^3/s)
STA 0+000	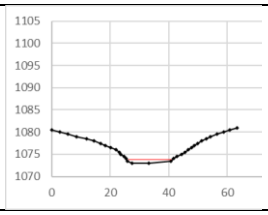		7.97	12.14	0.06	24.58	24.83
STA 0+050	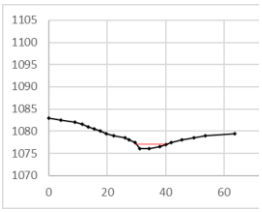		7.80	9.14	0.04	23.39	24.87
STA 0+100	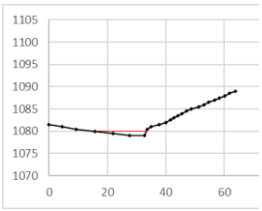		7.01	11.32	0.06	20.82	24.92
STA 0+150	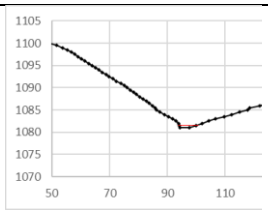		7.77	10.28	0.06	26.32	24.97
STA 0+200	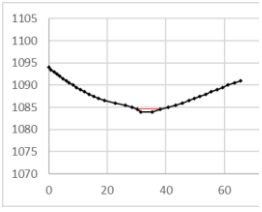		7.82	9.17	0.06	28.69	25.02

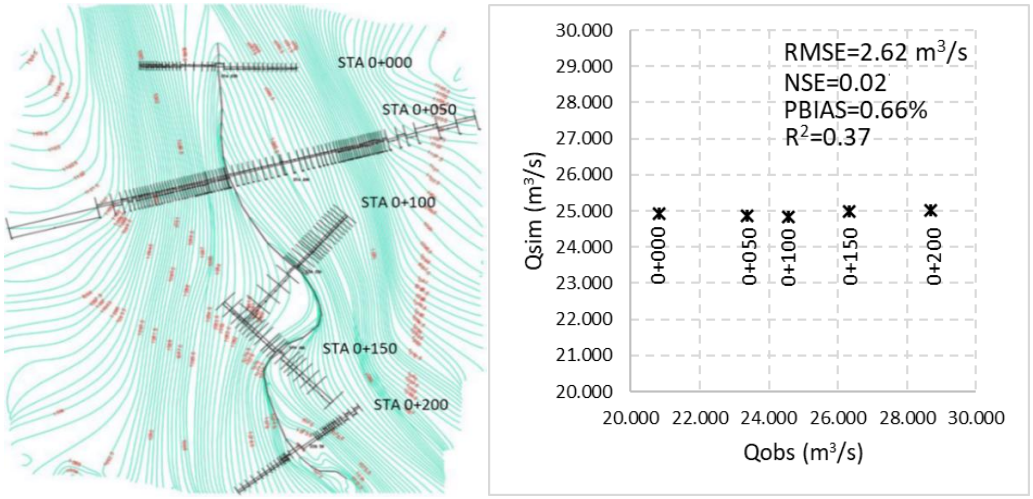

Figure 7 River bed contour from UAV (left); scatter plot of simulated runoff and discharge calculation from hydraulic observation (right)

Table 3 Flood simulation performance indices

Performance Rating	Reference			
	NSE	**PBIAS (%)**	**R^2**	**RMSE (m^3/s)**
Very good	0.75 < NSE ≤ 1.00	PBIAS < ±10	$R^2 \geq 0.5$	
Good	0.65 < NSE ≤ 0.75	±10 ≤ PBIAS < ±15		
Satisfactory	0.50 < NSE ≤ 0.65	±15 ≤ PBIAS < ±25		
Unsatisfactory	NSE ≤ 0.50	PBIAS > ±25	$R^2 < 0.5$	
Results	**0.02**	**0.66**	**0.37**	**2.62 m^3/s**
Performance	**Unsatisfactory**	**Very good**	**Unsatisfactory**	**Moderate**

Note: Performance thresholds follow Moriasi et al. (2007). NSE = Nash–Sutcliffe Efficiency; PBIAS = Percent Bias; R^2 = coefficient of determination; RMSE = Root Mean Square Error

Table 3 summarizes the flood simulation performance indices. The Root Mean Square Error (RMSE) of 2.62 m^3/s indicated moderate differences between simulated and observed discharge. The Nash–Sutcliffe Efficiency (NSE) of 0.02 reflected poor simulation skill in capturing temporal flow variability, indicating that the model performs only marginally better than a mean-flow benchmark. The coefficient of determination (R^2) of 0.37 further confirmed that the model explains a limited proportion of the observed discharge variance. Despite these limitations, the Percent Bias (PBIAS) of 0.66% indicated that the model is nearly unbiased in estimating total runoff volume, which is the primary input to the MUSLE sediment yield calculation. Since MUSLE relies on runoff volume and peak discharge rather than continuous flow time series, the poor temporal accuracy does not invalidate the sediment yield estimates for the design storm event analyzed here. Nevertheless, the results highlight the need for multi-event calibration and spatially distributed data to improve temporal accuracy in future applications.

The application of the Manning equation presented several limitations that affected simulation accuracy. First, the analysis relied on only five cross-sectional points from UAV surveys, providing insufficient spatial resolution to represent complex river morphologies. Second, flood marks may have faded or shifted in the weeks between the event and the survey, introducing uncertainty in identifying the exact peak water level. Third, hydraulic modeling was conducted for only a single flood event rather than a time series, limiting generalizability. Finally, the Manning roughness coefficient was assumed rather than calibrated against measured data.

4.3 Climate Change Analysis

Climate change projections were analyzed by comparing rainfall trends across seven consecutive five-year periods: 2026–2030, 2031–2035, 2036–2040, 2041–2045, 2046–2050, 2051–2055, and 2056–2060. The projections were derived from the CESM2 model under four shared socioeconomic pathway (SSP) scenarios — SSP1-2.6, SSP2-4.5, SSP3-7.0,

and SSP5-8.5 — representing a range of emission assumptions from low to very high. Figure 8 presents the slope of precipitation trends, expressed as the change in precipitation per year, across all four scenarios and all seven periods.

The trend and magnitude of precipitation change varied considerably depending on the scenario. Higher-emission scenarios (SSP3-7.0 and SSP5-8.5) tended to show greater variability across periods. Scenario SSP5-8.5 exhibited the strongest positive precipitation trend overall, suggesting the greatest potential increase in rainfall intensity or volume over the projection period. However, in the final projection period (2056–2060), the SSP2-4.5 scenario produced the highest positive precipitation trend slope, making it the wettest scenario at the 2060 horizon. Therefore, flooding and sediment transport were analyzed using the CESM2 SSP2-4.5 scenario for the purposes of this study.

Figure 9 illustrates the spatial distribution of annual average precipitation for the years 2030 and 2060 under the SSP2-4.5 scenario. A comparison of the two maps shows that the year 2060 experiences more intense rainfall than 2030, indicated by a transition to darker colors associated with higher precipitation rates of 6–10 mm/day. Higher precipitation zones expand notably in the middle-south region, where the study area is located, indicating an overall shift towards a wetter climate in this part of East Java.

Looking ahead to the 2051–2060 period, climate change projections indicate a significantly heightened risk of flooding even under the assumption that land use remains constant. Under the CESM2 SSP2-4.5 scenario, design rainfall is projected to increase from the current baseline of 124.67 mm/day to 153.88 mm/day — a rise of approximately 23.4 %. The projected peak runoff discharge is estimated to reach 30.83 m^3/s, representing a substantial increase compared to the 2025 baseline of 24.97 m^3/s.

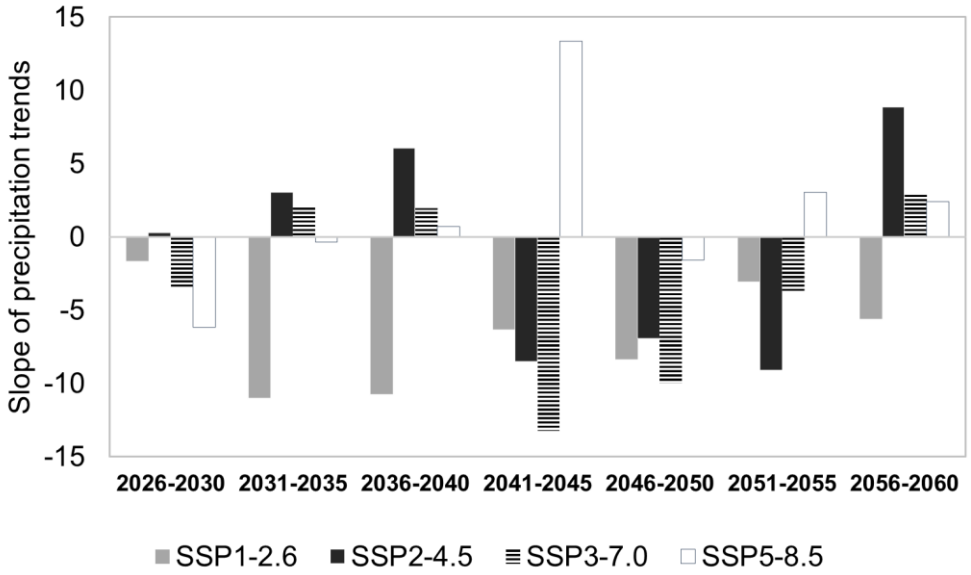

Figure 8 Trend of the precipitation trend slope across 5-year periods from 2026 to 2060 under four CESM2 SSP scenarios.

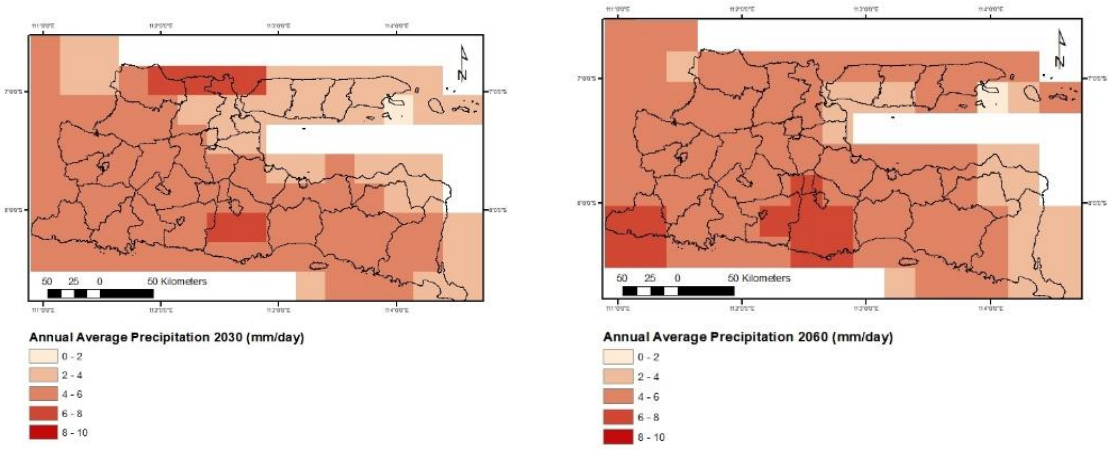

Figure 9 Comparison of annual average precipitation in 2030 (left) and 2060 (right) using the SSP2-4.5 scenario.

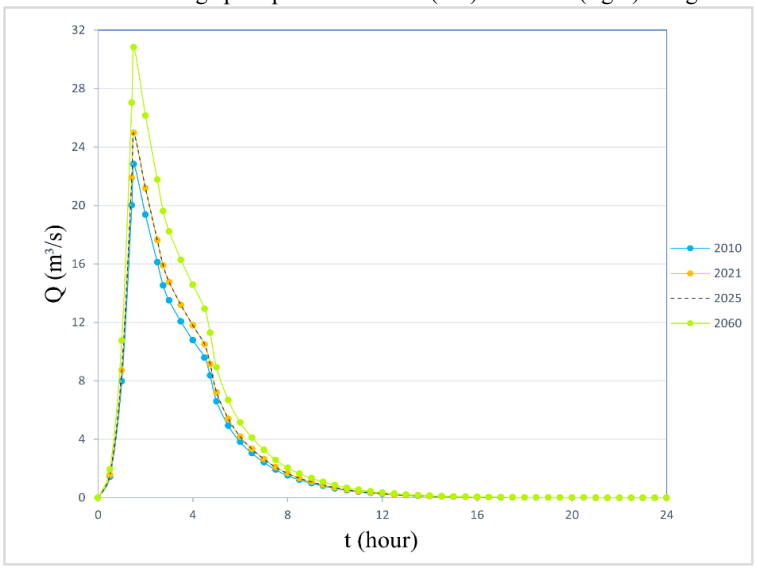

Figure 10 Simulated flood hydrographs for 2010, 2021, and 2025 land use conditions, and under the 2060 climate change projection.

Figure 10 presents a comparison of simulated flood hydrographs for the 2010, 2021, and 2025 land use conditions alongside the 2060 climate change projection, clearly illustrating the progressive increase in peak discharge across scenarios. These findings underscore that climate change alone may significantly amplify flood hazards over the next three decades, independent of any additional land use changes.

4.4 Erosion Rate Estimation

According to the soil properties in the catchment area — categorized as highly plastic clay, poorly aggregated, and containing some organic material — the soil erodibility factor (K) was determined to be 0.44. The slope angle of the watershed ranges from 1.02% to 121.9%, as shown in Figure 11. The average slope angle was 47.60% (25.45°), determined by averaging grid values across the basin. The slope length (λ) was 71.60 m, representing the horizontal distance from the point where overland flow begins to the point where the slope decreases sufficiently for flow to enter a channel. Based on these parameters, the LS factor was calculated to be 9.

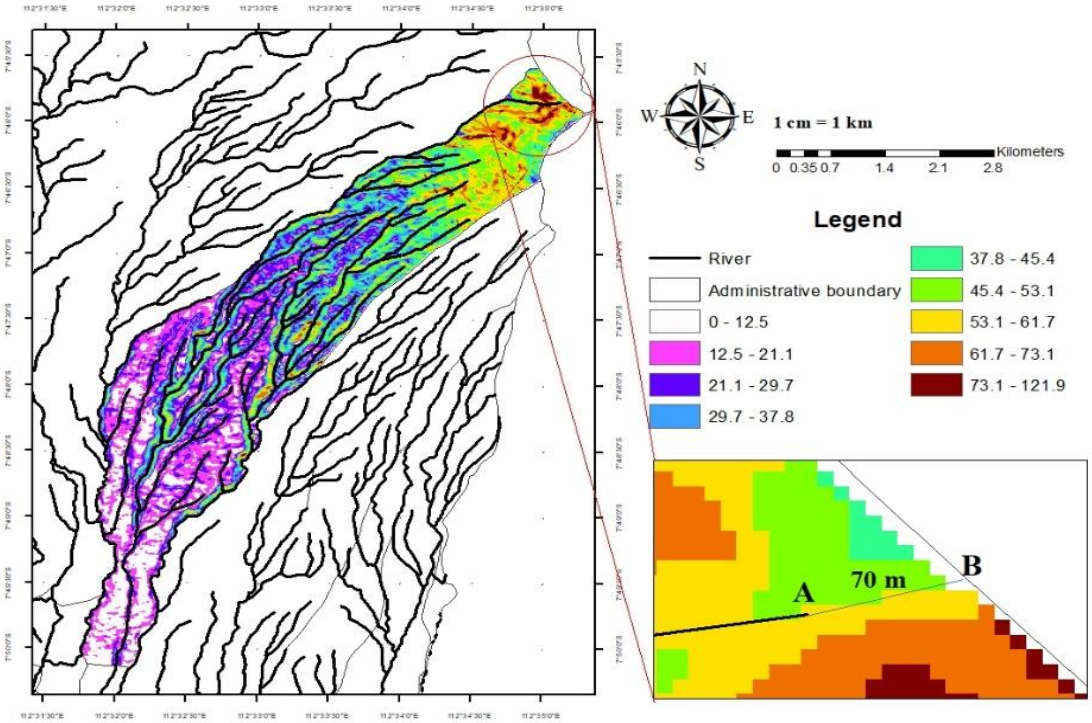

Figure 11 Slope angle (%) and the stream network

The cropping management factor (C) for the study area was determined as a weighted combination across land use types: housing (0), plantation and broadleaf-covered surfaces (0.011), fields and shrubland (0.011), grass and tall weeds (0.011), and forest (0.001), following the guidelines of Wischmeier and Smith (1978). The erosion control practice factor (P) was set at 0.60.

Using the verified peak discharge and the calculated time of concentration, the runoff volume for a single flood event under 2021 land use conditions was 27,190.96 m³. The estimated sediment yield from this single erosion event was approximately 101.94 tons. The relatively high sediment yield highlights the significant impact of storm events on soil degradation and underscores the importance of implementing effective soil and water conservation measures. Under 2010 land use conditions, the designed runoff volume was 24,577.71 m³, yielding a sediment yield of 75.21 tons. Under the 2060 climate change projection (SSP2–4.5 scenario), the runoff volume rose substantially to 34,421.95 m³, generating a sediment yield of 129.05 tons for a single flood event. Table 4 presents a comprehensive comparison of flood, erosion, and sedimentation quantities across all land use and climate change scenarios.

Figure 12 presents a sensitivity analysis examining the influence of rainfall return period (T_r) and runoff coefficient (C) on peak discharge. Figure 12 (left) demonstrates that as the rainfall return period increased from 6.25 to 400 years, peak discharge increased substantially, reflecting the non-linear nature of hydrological responses to extreme rainfall events. This underscores the disproportionate increase in flood hazard associated with rarer but more intense events, supporting the need for robust design standards in flood mitigation infrastructure. Figure 12 (right) shows that as the runoff coefficient increased from 0.23 to 0.31 — simulating the effect of land use changes such as urbanization or deforestation — both peak discharge and the steepness of the rising limb increased, indicating faster and more intense runoff generation.

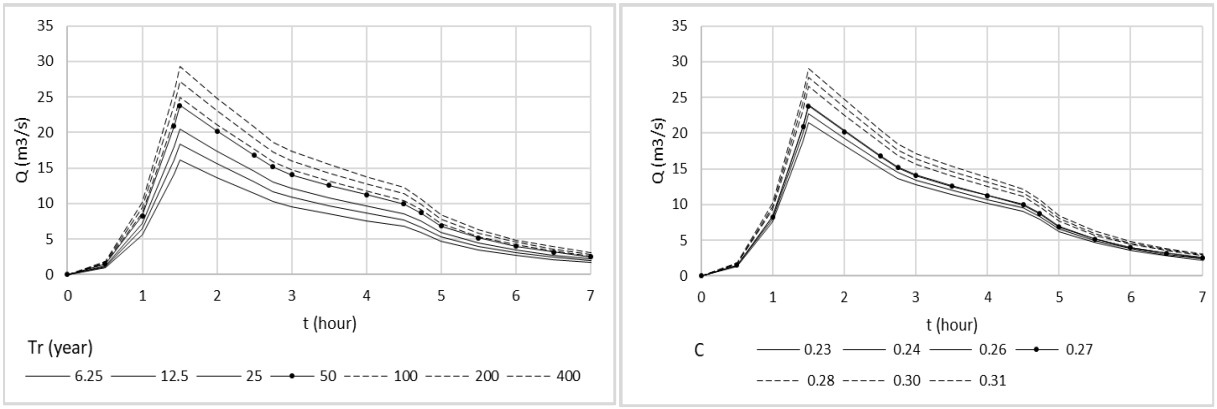

Figure 12 Sensitivity analysis of changing the rainfall return period and runoff coefficient to discharge.

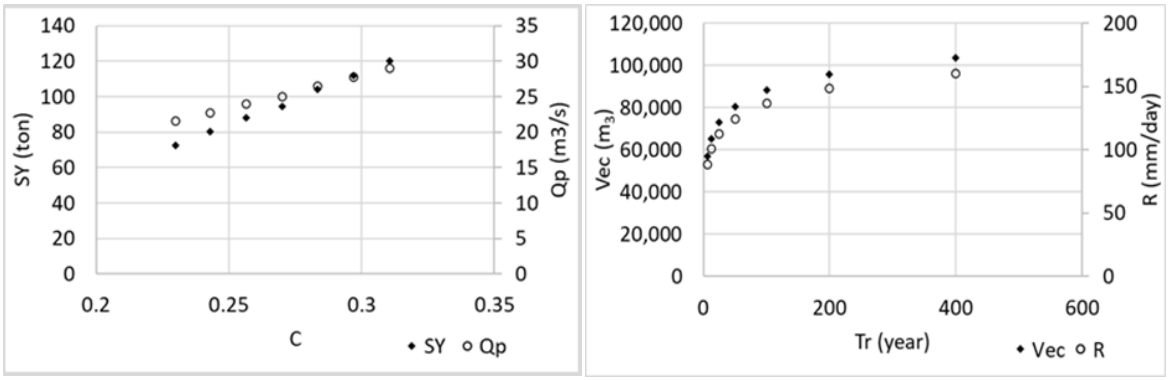

Figure 13 Sensitivity analysis of changing the rainfall return period to erosion rate and sediment volume

Table 4 Comparison of flood, erosion, and sedimentation quantity under different land use and climate change scenarios.

	Variable	Unit	2010 Land Use	2021 Land Use	2060 Climate Change Projection
*C*r	Runoff Coefficient		0.24	0.27	0.27
*C*m	Cropping Management Factor		0.01	0.01	0.01
P	Erosion Control Practice Factor		0.60	0.60	0.60
R	Maximum Daily Rainfall	mm/day	124.67	124.67	153.88
q_p	Peak Runoff Rate	m^3/s	22.82	24.97	30.83
SY	Sediment Yield	tons	75.21	101.94	129.05
V_{ec}	Volume of Sediment Carried	m^3	80,596.71	80,596.74	99,484.95

4.5 Sediment Volume Analysis

Based on the topographical map, the channel gradient of the Kricik River is 0.06 (3.38°). The critical gradient for debris flow initiation was calculated to be 0.01 from the debris mass density value. Since the actual channel gradient exceeded the critical gradient, the flow conditions met the criteria for debris flow. As the channel gradient was below 20°, the debris flow concentration (Cd) was determined using Equation 14, yielding a result of 0.31.

The volume of sediment transportable by debris flow, triggered by the design rainfall with a 50-year return period under 2021 land use conditions, was estimated at 80,596.71 m³. Under the projected 2060 climate conditions based on the SSP2–4.5 scenario, this volume increased to 99,484.95 m³. Table 4 presents a comprehensive comparison of flood, erosion, and sedimentation quantities across all land use and climate change scenarios considered in this study.

Figure 13 presents a sensitivity analysis examining the influence of the runoff coefficient and rainfall return period on erosion rate and sediment volume. Figure 13 (left) shows a clear positive

correlation: as the runoff coefficient increased from 0.23 to 0.31, the erosion rate increased from approximately 60 tons to approximately 120 tons. A higher runoff coefficient reflects a greater proportion of rainfall becoming surface runoff, which intensifies the erosive power of water and results in higher sediment yield. Figure 13 (right) shows the effect of the rainfall return period on sediment volume. As the return period extended from 6.25 to 400 years, sediment volume steadily increased, with the steepest growth occurring below the 100-year return period.

5. Discussion

Table 4 compares the quantities of flooding, erosion, and sedimentation across several land use and climate change scenarios based on modeling results. Under 2021 land use conditions, the watershed exhibited a moderate increase in hydrological and sedimentary responses to the 50-year design rainfall event compared to 2010 conditions. Although rainfall intensity was assumed to remain constant, peak discharge increased and sediment yield rose, indicating a heightened flash flood risk. This alteration is associated with the expansion of urban areas, the reduction of forest cover, and the increase in impermeable surfaces. These factors contribute to reduced infiltration and accelerated flash flood generation (Prokešová et al., 2022). Forests are essential for soil stabilization and the reduction of surface discharge through canopy interception, root reinforcement, and the accumulation of organic matter. The conversion of agricultural or forested land to urban settlements has been shown extensively to increase sediment mobilization and interfere with natural hydrological processes (Acharya et al., 2021). These findings align with research indicating that alterations in land use substantially modify runoff and sediment output (Zhou et al., 2010), even under steady rainfall conditions. The erosion rate in this context underscores the necessity for erosion control and sustainable watershed management measures.

In the MUSLE, the term $(Q \times q_p)^{0.56}$ reflects hydrological erosivity, where runoff volume (Q in m^3) and peak runoff rate (q_p in m^3/s) together represent the erosive force of the runoff. Runoff volume is a crucial hydrological input representing the total amount of water that flows over the land surface during a storm event and contributes to erosion. As the volume of water moving across the land increases, so does its capacity to erode and transport sediments downslope into waterways. In the erosion simulation results depicted in Table 4, a 9% change in the peak runoff rate led to a 36% change in sediment yield. This nonlinear relationship is due to the cropping management factor (C) and the erosion control practice factor (P). Due to changes in land use categories, the equivalent C and P values also changed based on the new land use composition. In a comparable tropical context, Odongo et al. (2013) found that a 9% increase in peak discharge led to a 4% rise in sediment transport in the upper Malewa Catchment, Kenya. A relevant study by An et al. (2016) conducted a sensitivity analysis of MUSLE parameters in Chinese watersheds and found that sediment yield was most sensitive to P, followed by LS, C, and q_p. The current study aligns partially with these results, reaffirming that effective land cover strategies and topographic conditions play a dominant role in sediment yield estimation, while hydrological parameters such as q_p have a comparatively smaller, yet still notable, impact.

Regarding the sediment volume carried by a flood event, an interesting result was observed: despite the increase in peak discharge, the sediment volume remained relatively steady. The multiplication of maximum daily rainfall with catchment area (Eq. 15) represents the total volume of rainfall input over the basin, which is directly related to discharge. The empirical formula of Mizuyama (2008) does not include a runoff coefficient, which reflects land use and infiltration capacity; rather, variations in land use are implicitly captured through rainfall–runoff interactions in this empirical rainfall-driven sediment dynamics model. Variations in land use are thus implicitly captured through rainfall–runoff interactions rather than being modelled explicitly.

According to the 2060 climate change projections based on the SSP2-4.5 scenario, the river basin shows a significant increase in hydrological response and sediment transport capacity. Compared to the conditions of 2010, 2021, and 2025, the projected rainfall intensity is expected to increase by 23%. This result is in line with the Intergovernmental Panel on Climate Change (IPCC) Sixth Assessment Report (2023), which reports increases in rainfall intensity and frequency under medium-range emission scenarios in numerous tropical regions. The findings suggest that the erosion rate will be significantly higher under the future climate conditions. The results are consistent with the research conducted by Westra et al. (2013), which discussed the correlation between increasing atmospheric moisture, warming, and

intensified rainfall-induced erosion. Integrating climate adaptation techniques into watershed and land use planning is necessary to alleviate the expected increase in erosion risk and sediment-related threats caused by shifting climatic conditions (Adeyeri et al., 2024).

In general, steep, narrow catchments, particularly those with radial-dendritic drainage patterns, are prone to severe geomorphological hazards due to their rapid response to storm onset, high energy, and capacity for material transport. Sub-catchments of the upper Brantas River basin pose sudden flood risks, combining hydrological surges with mass sediment transport, such as the event that unexpectedly occurred on November 4, 2021. Flash floods are among the most destructive hydrometeorological hazards, often occurring with minimal warning. This study and the subsequent discussions suggest two primary factors for the observed phenomena: first, human-induced land use changes, as the analysis implies; and second, triggers from hydrological elements—such as rainfall intensity, accumulated precipitation, and antecedent soil moisture—that reach critical thresholds. However, flash flood systems remain complex, involving nonlinear responses between rainfall, land surface conditions, and watershed characteristics. Further study utilizing robust, physically based modeling or observed data-driven approaches is needed to improve early warning systems and reduce the risk of flash flood impacts.

6. Conclusion

This study demonstrates that climate change and land use change significantly affect the hydrological response and sediment dynamics in the Kricik River Basin, a vital upstream sub-basin of the Upper Brantas River system. Under 2010 land use conditions, the basin had a peak discharge of 22.82 m^3/s, a sediment yield of 75.21 tons, and a transportable sediment volume of 80,596.71 m^3 during a 50-year design rainfall event of 124.67 mm/day. At the same rainfall intensity, 2021 conditions showed a peak discharge of 24.97 m^3/s, a sediment yield of 101.94 tons, and a sediment flow volume of 80,596.71 m^3. Alterations in land use, particularly the expansion of urban areas and the transformation of forests and plantations into fields, grasslands, and shrublands, were likely the primary contributors to these increases. These changes have resulted in larger impermeable surfaces, reduced vegetation cover, and increased surface discharge and soil loss. Furthermore, the 2060 climate change projection (SSP2-4.5) exhibited the most severe impact, with a 23% increase in rainfall intensity compared to current scenarios, resulting in 153.88 mm/day of daily rainfall. This condition led to a peak discharge of 30.83 m^3/s, a debris flow volume of 99,484.95 m^3, and a sediment yield of 129.05 tons. This study indicates that climate intensification and land use changes exacerbate flood threats, erosion risks, and sediment transport in watersheds. Adaptive watershed management is required, including sustainable land use planning, forest preservation, and erosion mitigation methods, to promote resilience to future environmental challenges in the Upper Brantas Basin. Future research will focus on utilizing distributed hydrological models to provide a more detailed representation of catchment responses by incorporating additional climatological parameters. Further investigation is also planned to incorporate projections of anthropogenic factors in conjunction with climate change scenarios.

7. Acknowledgements

The authors express their sincere gratitude to Politeknik Negeri Malang for providing research funding through its institutional grant program. Appreciation is also extended to the National Research and Innovation Agency (BRIN), Indonesia, for providing access to essential data.

8. Abbreviation List

Abbreviation	Full Term
CESM2	Community Earth System Model version 2
FAO	Food and Agriculture Organization
GIS	Geographic Information System
ha	hectare
IDF	Intensity-Duration-Frequency
IPCC	Intergovernmental Panel on Climate Change
MUSLE	Modified Universal Soil Loss Equation
NSE	Nash–Sutcliffe Efficiency
PBIAS	Percent Bias
RMSE	Root Mean Square Error
SSP	Shared Socioeconomic Pathway
UAV	Unmanned Aerial Vehicle

9. CRediT Statement

Ratih Indri Hapsari: Conceptualization, Methodology, Writing – original draft.
Fidia Sabilla Putri: Formal analysis (sediment and hydrology data analysis).

Winda Harsanti: Data curation, Formal analysis (topography data analysis)
Ginaldi Ari Nugroho: Data curation (meteorological data collection)
Amalia Nurlatifah: Data curation (hydrological data collection)
Asif Awaludin: Writing – review & editing (proofreading)
Hazruwani Binti A Halim: Writing – review & editing (English checking)

10. References

Acharya, B. S., Bhandari, M., Bandini, F., Pizarro, A., Perks, M., Joshi, D. R., ... & Sharma, S. (2021). Unmanned aerial vehicles in hydrology and water management: Applications, challenges, and perspectives. *Water Resources Research*, *57*(11), Article e2021WR029925. https://doi.org/10.1029/2021WR029925

Adeyeri, O. E., Folorunsho, A. H., Adeliyi, T. E., Ayegbusi, K. I., Akinsanola, A. A., Ndehedehe, C. E., ... & Babalola, T. E. (2024). Climate change is intensifying rainfall erosivity and soil erosion in West Africa. *Science of the Total Environment*, *955*, Article 177174. https://doi.org/10.1016/j.scitotenv.2024.177174

An, L. S., Liao, K. H., Zhou, B. H., Pan, W., & Chen, Q. (2016). Global sensitivity analysis of the parameters of the modified universal soil loss equation. *Applied Ecology and Environmental Research*, *14*(4), 505-514. https://doi.org/10.15666/aeer/1404_505514

Borrelli, P., Alewell, C., Alvarez, P., Anache, J. A. A., Baartman, J., Ballabio, C., ... & Panagos, P. (2021). Soil erosion modelling: A global review and statistical analysis. *Science of the Total Environment*, *780*, Article 146494. https://doi.org/10.1016/j.scitotenv.2021.146494

Danabasoglu, G., Lamarque, J. F., Bacmeister, J., Bailey, D. A., DuVivier, A. K., Edwards, J., ... & Strand, W. G. (2020). The community earth system model version 2 (CESM2). *Journal of Advances in Modeling Earth Systems*, *12*(2), Article e2019MS001916. https://doi.org/10.1029/2019MS001916

Dash, S. S., & Maity, R. (2023). Effect of climate change on soil erosion indicates a dominance of rainfall over LULC changes. *Journal of Hydrology: Regional Studies*, *47*, Article 101373. https://doi.org/10.1016/j.ejrh.2023.101373

Faksomboon, B. (2023). Predicting spatial land use and land cover change using an integrated mathematical model in the Khlong Nam Lai Watershed, Kamphaeng Phet Province, Thailand. *EnvironmentAsia*, *16*(1), 16-27. https://doi.org/10.14456/EA.2023.2

Hernina, R., Martono, D. N., Koestoer, R. H., & Soesilo, T. E. B. (2024). Land use/land cover simulation scenarios in Bogor and Karawang regencies' border area, Indonesia, using GIS-based multi-stakeholder tourism analysis. *EnvironmentAsia*, *17*(1), 69-82. https://doi.org/10.14456/ea.2024.6

Hidayat, A., Limantara, L. M., Soetopo, W., & Sisinggih, D. (2022). Alpha parameter modeling of Nakayasu synthetic unit hydrograph based on the watershed shape factor. *Journal of Hunan University Natural Sciences*, *49*(1), 31–37. https://doi.org/10.55463/issn.1674-2974.49.1.5

Intergovernmental Panel on Climate Change. (2023). *Climate change 2023: Synthesis report. Contribution of Working Groups I, II and III to the Sixth Assessment Report of the Intergovernmental Panel on Climate Change* (Core Writing Team, H. Lee, & J. Romero, Eds.). IPCC. https://doi.org/10.59327/IPCC/AR6-9789291691647

Kang, M. S., Goo, J. H., Song, I., Chun, J. A., Her, Y. G., Hwang, S. W., & Park, S. W. (2013). Estimating design floods based on the critical storm duration for small watersheds. *Journal of Hydro-Environment Research*, *7*(3), 209-218. https://doi.org/10.1016/j.jher.2013.01.003

Kulkarni, S. (2021). Climate change, soil erosion risks, and nutritional security. *Climate Change and Resilient Food Systems: Issues, Challenges, and Way Forward*, 219-244. https://doi.org/10.1007/978-981-33-4538-6_8

Lagogiannis, S., & Dimitriou, E. (2021). Discharge estimation with the use of unmanned aerial vehicles (UAVs) and hydraulic methods in shallow rivers. *Water*, *13*(20), Article 2808. https://doi.org/10.3390/w13202808

Leh, M., Bajwa, S., & Chaubey, I. (2013). Impact of land use change on erosion risk: An integrated remote sensing, geographic information system and modeling methodology. *Land Degradation & Development*, *24*(5), 409-421. https://doi.org/10.1002/ldr.1137

Li, N., Zhang, Y., Wang, T., Li, J., Yang, J., & Luo, M. (2022). Have anthropogenic factors

mitigated or intensified soil erosion over the past three decades in South China?. *Journal of Environmental Management*, *302*, Article 114093. https://doi.org/10.1016/j.jenvman.2021.114093

Mizuyama, T. (2008). Structural countermeasures for debris flow disasters. *International Journal of Erosion Control Engineering*, *1*(2), 38-43. https://doi.org/10.13101/ijece.1.38

Mohammadi, M., Khaledi Darvishan, A., Spalevic, V., Dudic, B., & Billi, P. (2021). Analysis of the impact of land use changes on soil erosion intensity and sediment yield using the intero model in the talar watershed of Iran. *Water*, *13*(6), Article 881. https://doi.org/10.3390/w13060881

Moriasi, D. N., Arnold, J. G., Van Liew, M. W., Bingner, R. L., Harmel, R. D., & Veith, T. L. (2007). Model evaluation guidelines for systematic quantification of accuracy in watershed simulations. *Transactions of the ASABE*, *50*(3), 885-900. https://doi.org/10.13031/2013.23153

Nakayasu, Y. (1956). *On the unit graph of Japanese river floods*. Ministry of Construction, 7th Technical Research Meeting Report. Retrieved from https://www.jstage.jst.go.jp/browse/prohe1956/1/0/_contents/-char/ja

Nassor, S. H., Matlan, S. J., Taha, N. A., & Mukhlisin, M. (2025). Influence of hydraulic properties on the slope stability of unsaturated soil from the garinono formation in Sabah. *Journal of Current Science and Technology*, *15*(1), Article 88. https://doi.org/10.59796/jcst.V15N1.2025.88

Odongo, V. O., Onyando, J. O., Mutua, B. M., & Becht, R. (2013). Sensitivity analysis and calibration of the Modified Universal Soil Loss Equation (MUSLE) for the upper Malewa catchment, Kenya. *International Journal of Sediment Research*, *28*(3), 368-383. https://doi.org/10.1016/S1001-6279(13)60047-5

Prokešová, R., Horáčková, Š., & Snopková, Z. (2022). Surface runoff response to long-term land use changes: Spatial rearrangement of runoff-generating areas reveals a shift in flash flood drivers. *Science of the Total Environment*, *815*, Article 151591. https://doi.org/10.1016/j.scitotenv.2021.151591

Pumpuang, A., & Aobpaet, A. (2024). Evolution pattern of land subsidence using InSAR Time-series analysis in Bangkapi, Bangkok, Thailand. *Journal of Current Science and Technology*, *14*(3), Article 49. https://doi.org/10.59796/jcst.V14N3.2024.49

Putri, F. S., Hapsari, R. I., & Harsanti, W. (2022). Planning of a sabo dam on the Kricik River for flood control in Bumiaji District, Batu City *(in Indonesian)*. *Jurnal Online Skripsi Manajemen Rekayasa Konstruksi (JOS-MRK)*, *3*(4), 13–19. https://jurnal.polinema.ac.id/index.php/jos-mrk/article/view/1081

Ray, R., Samui, P., & Roy, L. B. (2023). Reliability analysis of a shallow foundation on clayey soil based on settlement criteria. *Journal of Current Science and Technology*, *13*(1), 91-106. https://doi.org/10.14456/jcst.2023.9

Shu, Y., & Lam, N. S. (2011). Spatial disaggregation of carbon dioxide emissions from road traffic based on multiple linear regression model. *Atmospheric Environment*, *45*(3), 634-640. https://doi.org/10.1016/j.atmosenv.2010.10.037

Takahashi, T. (1977). A mechanism of occurrence of mud-debris flow and their characteristics in motion. *Annuals, Disaster Prevention Research Institute Kyoto University*, *20*, 405-432.

Takahashi, T. (1978). The occurrence and flow mechanism of debris flow. *Soil Mechanics and Foundation Engineering*, *26*(6), 45-50.

Takahashi, T. (2001). Process of occurrence, flow and deposition of viscous debris flow. *River, coastal and estuarine morphodynamics*. Berlin, Heidelberg: Springer Berlin Heidelberg.

Westra, S., Alexander, L. V., & Zwiers, F. W. (2013). Global increasing trends in annual maximum daily precipitation. *Journal of Climate*, *26*(11), 3904-3918. https://doi.org/10.1175/JCLI-D-12-00502.1

Williams, J. R. (1975). *Sediment-yield prediction with universal equation using runoff energy factor*. Retrieved from https://www.semanticscholar.org/paper/Sediment-yield-prediction-with-Universal-Equation-Williams/a9bc4612310f980c973575cbf86c63b77a01ace1

Wischmeier, W. H., & Smith, D. D. (1978). *Predicting rainfall erosion losses: A guide to conservation planning* (Agriculture Handbook No. 537). U.S. Department of Agriculture. Retrieved from https://books.google.co.th/books/about/Predicting_Rainfall_Erosion_Losses.html?id=rRAUAAAAYAAJ&redir_esc=y

Wiwoho, B. S., McIntyre, N., & Phinn, S. (2024). Assessing future land-uses under planning scenarios: A case study of The Brantas River

Basin, Indonesia. *Environmental Challenges*, *15*, Article 100873. https://doi.org/10.1016/j.envc.2024.100873

Xiao, T., Ran, F., Li, Z., Wang, S., Nie, X., Liu, Y., ... & Feng, S. (2023). Sediment organic carbon dynamics response to land use change in diverse watershed anthropogenic activities. *Environment International*, *172*, Article 107788. https://doi.org/10.1016/j.envint.2023.107788

Yang, D., Kanae, S., Oki, T., Koike, T., & Musiake, K. (2003). Global potential soil erosion with reference to land use and climate changes. *Hydrological Processes*, *17*(14), 2913-2928. https://doi.org/10.1002/hyp.1441

Zhou, G., Wei, X., Luo, Y., Zhang, M., Li, Y., Qiao, Y., ... & Wang, C. (2010). Forest recovery and river discharge at the regional scale of Guangdong Province, China. *Water Resources Research*, *46*(9), Article W09503. https://doi.org/10.1029/2009WR008829